Title

Three-dimensional whole-brain simultaneous T1, T2, and T1ρ quantification using MR Multitasking: Method and initial clinical experience in tissue characterization of multiple sclerosis

Journal

Magnetic Resonance in Medicine, 85(4)

ISSN

0740-3194

Authors

Ma, Sen
Wang, Nan
Fan, Zhaoyang
et al.

Publication Date

2021-04-01

DOI

10.1002/mrm.28553

Peer reviewed

HHS Public Access

Author manuscript

Magn Reson Med. Author manuscript; available in PMC 2022 April 01.

Published in final edited form as:

Magn Reson Med. 2021 April ; 85(4): 1938–1952. doi:10.1002/mrm.28553.

Three-Dimensional Whole-Brain Simultaneous T1, T2, and T1ρ Quantification using MR Multitasking: Method and Initial Clinical Experience in Tissue Characterization of Multiple Sclerosis

Sen Ma[1,2], **Nan Wang**[1,2], **Zhaoyang Fan**[1,2], **Marwa Kaisey**[3], **Nancy L. Sicotte**[3], **Anthony G. Christodoulou**[1,2], **Debiao Li**[1,2,*]

[1.]Biomedical Imaging Research Institute, Cedars-Sinai Medical Center, Los Angeles, CA, USA

[2.]Department of Bioengineering, University of California, Los Angeles, Los Angeles, CA, USA

[3.]Department of Neurology, Cedars-Sinai Medical Center, Los Angeles, CA, USA

Abstract

Purpose: To develop a 3D whole-brain simultaneous T1/T2/T1ρ quantification method with MR Multitasking that provides high quality, co-registered multiparametric maps in 9min.

Methods: MR Multitasking conceptualizes T1/T2/T1ρ relaxations as different time dimensions, simultaneously resolving all three dimensions with a low-rank tensor image model. The proposed method was validated on a phantom and in healthy volunteers, comparing quantitative measurements against corresponding reference methods and evaluating the scan-rescan repeatability. Initial clinical validation was performed in age-matched relapsing-remitting multiple sclerosis (RRMS) patients to examine the feasibility of quantitative tissue characterization and to compare with the healthy control cohort. The feasibility of synthesizing six contrast-weighted images was also examined.

Results: Our framework produced high quality, co-registered T1/T2/T1ρ maps that closely resemble the reference maps. Multitasking T1/T2/T1ρ measurements showed substantial agreement with reference measurements on the phantom and in healthy controls. Bland-Altman analysis indicated good in vivo repeatability of all three parameters. In RRMS patients, lesions were conspicuously delineated on all three maps and on four synthetic weighted images (T2-weighted, T2-FLAIR, double inversion recovery, and a novel "T1ρ-FLAIR" contrast). T1 and T2 showed significant differences for normal appearing white matter between patients and controls, while T1ρ showed significant differences for normal appearing white matter, cortical gray matter, and deep gray matter. The combination of three parameters significantly improved the differentiation between RRMS patients and healthy controls, as compared to using any single parameter alone.

Conclusion: MR Multitasking simultaneously quantifies whole-brain T1/T2/T1ρ and is clinically promising for quantitative tissue characterization of neurological diseases such as MS.

[*]indicates corresponding author. Debiao Li, address: 8700 Beverly Blvd, PACT 400, Los Angeles, CA 90048, debiao.li@cshs.org, phone: 3104237743.

Keywords

Simultaneous T1/T2/T1ρ mapping; MR Multitasking; low-rank tensor; quantitative tissue characterization; multiple sclerosis

1. Introduction

MRI relaxometry reveals biological tissue properties by characterizing the excited spin dynamics in the presence of external magnetic fields. For example, quantifying T1/T2 in the brain is clinically promising for tissue characterization, early detection, staging, and treatment monitoring of various brain tumors[1-4] and neurologic pathologies such as multiple sclerosis (MS)[5-9], Alzheimer's disease[10-12], Parkinson's disease[13-15], and more. One of the major benefits of quantitative measurements are their potential to be more sensitive and reproducible compared to conventional qualitative MRI. T1ρ is an emerging relaxometry mechanism described as the spin-lattice relaxation in the rotating frame, which measures the decay of the transverse magnetization in the presence of an external "spin-locking" B1 field[16]. The frequency of the spin-locking RF pulse for T1ρ imaging is usually in the range of kilohertz where the T1ρ relaxation process is maximized, as opposed to the Larmor frequency in the range of megahertz for conventional T1 and T2 imaging, making T1ρ more suitable to detect low-frequency motional biological processes such as protein exchange between macromolecules and extracellular water[16]. T1ρ is most commonly used in articular cartilage imaging so far, showing promise for early detection of subtle cartilage matrix degeneration of osteoarthritis patients due to its high sensitivity to the collagen-proteoglycan matrix damage[17-20]. A few studies have also explored the value of T1ρ in pathological activities of degenerative neurologic diseases and provided useful image biomarkers for the evaluation and early diagnosis of Alzheimer's disease[21,22], Parkinson's disease[23,24], stroke[25], and MS[26,27].

Despite the great potential of quantitative MR relaxometry to allow comprehensive evaluation of tissue states, multiparametric mapping of T1/T2/T1ρ is time-consuming and may be impractical in clinical settings. This is especially true for T1ρ imaging, which can be slow and inefficient due to the necessary delay time for magnetization restoration, the multiple spin-lock times, and the multiple spin-lock frequencies required. Moreover, if measured in separate acquisitions, these parameter maps may be subject to misalignment due to patient movement. Consequently, efficient and simultaneous quantification of multiple relaxation parameters is highly desirable for clinical practice.

Simultaneous T1/T2 mapping has been widely explored in the past two decades. DESPOT1/DESPOT2 employs the spoiled gradient echo and steady-state free precession acquisitions sequentially, showing superior performance of SNR efficiency compared to separate T1/T2 acquisitions[28]. MR fingerprinting demonstrates even better SNR efficiency than DESPOT1/DESPOT2 and has been validated in various clinical applications[29-31]. MR Multitasking models different image dynamics in a multidimensional tensor and explores signal correlation in a multidimensional subspace for multiparametric mapping[32], and has been used for various parameter combinations such as T1/T2 and T1/T2/ADC[32-34]. MAPSS

concatenates a series of T2 and T1ρ preparations for combined T2/T1ρ acquisition[35]. Simultaneous T1/T2/T1ρ mapping with MR Fingerprinting has recently been reported for 2D abdominal[36] and 2D knee imaging[37], but 3D techniques have not yet been reported.

In this work, we demonstrate simultaneous quantification of T1/T2/T1ρ with 3D whole-brain coverage in 9 minutes. Our framework conceptualizes the multiple relaxation processes (e.g., T1, T2, and T1ρ) as multiple time dimensions to establish a multidimensional image tensor. Accelerated imaging can be achieved by exploiting the strong spatiotemporal correlation throughout this tensor, which can be efficiently represented in a low dimensional subspace using a low-rank tensor[38] (LRT) image model. In addition to mapping, we also demonstrate the feasibility of generating six synthetic contrast-weightings from the T1/T2/T1ρ maps. Repeatability of quantitative measurements and the agreement with reference approaches are evaluated on a phantom and in healthy controls. Clinical validation is performed on a relapsing-remitting multiple sclerosis (RRMS) patient cohort, hypothesizing that each relaxometry mapping offers complementary tissue information and the integration of three parameters allows better detection and assessment of the degenerative pathologic progression in multiple sclerosis.

2. Methods

2.1. Pulse sequence design

The pulse sequence structure builds upon our previously developed Multitasking T1/T2 mapping sequence[32] by incorporating T1ρ components. It generates T1/T2/T1ρ contrasts by cycling through several B0- and B1-insensitive hybrid T2-preparation/inversion recovery (T2-IR) pulses with different durations τ and several B0- and B1-insensitive hybrid T1ρ-preparation/inversion recovery (T1ρ-IR) pulses with different spin-lock times τ_{SL}. The T2-IR pulse is modified from an adiabatic T2-preparation module[39], replacing the 90° tip-up pulse by a 90° tip-down pulse after refocusing to achieve the inversion effect[40]. The T1ρ-IR pulse follows a similar scheme: it is modified from a paired self-compensated T1ρ-preparation module[41], also replacing the 90° tip-up pulse by a 90° tip-down pulse after refocusing to achieve the inversion effect[42]. 3D FLASH excitations fill the entire recovery period between preparation pulses for data readouts. A detailed illustration of the pulse sequence and signal evolution is shown in Figure 1A-1C.

2.2. k-Space sampling

The data acquisition scheme is described in Figure 1D, where two interleaved subsets of k-space data are collected in a continuous acquisition. The imaging data ($\mathbf{d}_{img}$) are collected with a 3D Gaussian-density random Cartesian trajectory along both phase-encoding ($\mathbf{k}_y$) and partition-encoding ($\mathbf{k}_z$) directions. The subspace training data ($\mathbf{d}_{tr}$) are periodically embedded into the imaging data collection at the k-space center location (i.e., $\mathbf{k}_y = \mathbf{k}_z = 0$) every 8 readouts.

2.3. Low-rank tensor image model

We model the underlying image sequence as a 6-dimensional function $x(\mathbf{r}, n, \tau, \tau_{SL})$ with $\mathbf{r} = [x,y,z]$ indexing three spatial dimensions, while n, τ, and τ_{SL} index three time dimensions

characterizing the dynamic processes of T1 relaxation, T2 relaxation, and T1ρ relaxation respectively. This image function x lies in a high-dimensional space but is often highly structured due to the strong signal correlation along each dimension. As a result, x can be efficiently represented in any or all of four low-dimensional subspaces modeling the spatial distribution, T1 relaxation process, T2 relaxation process, and T1ρ relaxation process, respectively, where in each subspace, x can be represented as a linear combination of the basis functions spanning this subspace. In this sense, x can be decomposed into the combination of four sets of basis functions spanning the corresponding four subspaces[43,44]. In this work, we employ the Tucker form of decomposition[45]:

$$x(\mathbf{r}, n, \tau, \tau_{\mathrm{SL}}) = \sum_{i=1}^{I} u_i(\mathbf{r}) v_i(n, \tau, \tau_{\mathrm{SL}}) \tag{1}$$

$$v_i(n, \tau, \tau_{\mathrm{SL}}) = \sum_{j=1}^{J} \sum_{k=1}^{K} \sum_{l=1}^{L} c_{ijkl} w_j(n) p_k(\tau) q_l(\tau_{\mathrm{SL}}) \tag{2}$$

where $\{u_i(\mathbf{r})\}_{i=1}^{I}$ represents the spatial basis functions; $\{w_j(n)\}_{j=1}^{J}$, $\{p_k(\tau)\}_{k=1}^{K}$, and $\{q_l(\tau_{\mathrm{SL}})\}_{l=1}^{L}$ represent the temporal basis functions of the three time dimensions respectively; *I, J, K, L* represents the number of basis functions for each dimension; c_{ijkl} denotes the core tensor elements (the weights assigned to each combination of basis functions); and $\{v_j(n, \tau, \tau_{\mathrm{SL}})\}_{i=1}^{I}$ spans the multidimensional temporal subspace jointly modeling T1 relaxation, T2 relaxation, and T1ρ relaxation processes.

The image function x can be further represented in discretized form as a 4-way tensor $\mathcal{X}$ with elements $X_{ijkl} = x(\mathbf{r}_i, n_j, \tau_k, \tau_{\mathrm{SL},l})$. $\mathcal{X}$ is an LRT due to the linear dependency within x, as is indicated by Eqs. (1) and (2), and can be factorized as the tensor product of four factor matrices and a core tensor according to the Tucker form of tensor decomposition[45]. Therefore, the image model in Eqs. (1) and (2) becomes:

$$\mathcal{X} = \mathcal{V} \times_1 \mathbf{U} \tag{3}$$

$$\mathcal{V} = \mathcal{C} \times_2 \mathbf{W} \times_3 \mathbf{P} \times_4 \mathbf{Q} \tag{4}$$

where the tensor $\mathcal{V}$ has elements $V_{ijkl} = v_i(n_j, \tau_k, \tau_{\mathrm{SL},l})$ modeling the temporal dynamics and is itself and LRT; the factor matrix **U** contains spatial basis functions; the factor matrices **W**, **P**, **Q**, contain temporal basis functions spanning the three temporal subspaces corresponding to T1, T2, and T1ρ; $\mathcal{C} \in \mathbb{C}^{I \times J \times K \times L}$ is the core tensor with elements c_{ijkl} governing the interaction between different factor matrices; and $\times_i$ denotes the tensor i-mode product to perform the tensor form multiplication[43].

We note that the factor matrices and the core tensor have far fewer elements than the full image tensor $\mathcal{X}$, which significantly reduces the degrees of freedom for the LRT recovery problem, thus reducing the sampling requirements and accelerating the acquisition[32].

For clarity, we provide a detailed definition of the three time indices n, τ, and τ_{SL} here. The readout index is $n_j = j$=1,2,…,N denotes the readout index, where N is the number of readouts per recovery period; this indexes T1 recovery after a preparation pulse and is reset for each recovery period. The T2-IR duration τ is indexed by k=1,2,…,N_{T2IR}, where N_{T2IR} is the number of T2-IR pulses. This groups readout lines following the kth T2-IR preparation pulse duration τ_k; any readout lines which does not come after a T2-IR preparation pulse (i.e., they followed a T1ρ-IR preparation pulse) are assigned k=N_{T2IR}+1. Similarly, the T1ρ-IR duration τ_{SL} is indexed by l=1,2,…,$N_{T1\rho IR}$, where $N_{T1\rho IR}$ is the number of T1ρ-IR pulses. This groups all the readout lines following the lth T1ρ-IR preparation pulse duration $\tau_{SL,l}$; any readout lines which does not come after a T1ρ-IR preparation pulse (i.e., they follows a T2-IR preparation pulse) are assigned l=$N_{T1\rho IR}$+1. A detailed graphical illustration for mapping n, τ, and τ_{SL} to the pulse sequence diagram in Figure 1 is described in Supporting Information Figure S1.

2.4. Image reconstruction

MR Multitasking allows accelerated imaging as well as rapid and memory-efficient reconstruction by serially recovering the spatial and temporal factor matrices composing $\mathcal{X}$. Specifically, this can be achieved in two stages:

2.4.1 Multidimensional tensor subspace estimation—In this stage, we propose to estimate the factor matrices **W**, **P**, **Q**, as well as the core tensor $\mathcal{C}$. This can be achieved in a two-step process:

1) Predetermine the basis functions $\{w_j(n)\}_{j=1}^{J}$ for the T1 relaxation dimension. We generate a training dictionary of physically feasible IR-FLASH signal curves governed by the Bloch equations, with a range of feasible T1 values and B1 inhomogeneities, as demonstrated in our previous work[32]. Specifically, we use 101 T1 values logarithmically spaced between 100ms and 4000ms, 15 FLASH flip angles equally spaced between 0.5° to 7.5° controlling the effect of B1 inhomogeneities on the FLASH flip angle, and 21 efficiency factors controlling the combined effects of inversion efficiency and the T2 and T1ρ weightings, equally spaced between −1 (perfect inversion, zero T2 and T1ρ) to 0 (infinite T2 and T1ρ). Therefore, the dictionary comprises 31815 feasible signal curves. The T1 relaxation basis functions in **W** are estimated from the SVD of this training dictionary. Basis functions for the T2 and T1ρ relaxation dimensions are not predetermined due to the complexity of modeling B0 inhomogeneities and will instead be calculated from the training data in the second step.

2) Determine **P**, **Q**, $\mathcal{C}$. Using the known n, τ, τ_{SL} timings of the acquired data, the subspace training data $\mathbf{d}_{tr}$ can be reshaped into a 4-way training tensor $\mathcal{D}_{tr}$ in the (**k**, n, τ, τ_{SL})-space, where **k** indexes the k-space location. This training tensor covers various dynamic image contrast combinations experienced throughout the entire scan, but it doesn't cover all the contrast combinations. For example, it only covers the T1 weightings at n=8i+1 with i=0,1,…,N/8-1 corresponding to the subspace training data indices. We also perform abrupt motion identification using the subspace training data, and remove the training tensor elements corresponding to the motion indices[46]. As a result, this training tensor is

incomplete. A graphical illustration of the training tensor undersampling is shown in Supporting Information Figure S1. However, because the training tensor contains very limited spatial information and therefore has far fewer size than the image tensor, it can be efficiently recovered via a Bloch-constrained small-scale LRT completion problem:

$$\widehat{\mathscr{D}}_{\mathrm{tr}} = \arg\min_{\mathbf{D}_{\mathrm{tr},(2)} \in \mathrm{range}(\mathbf{W})} \|\mathbf{d}_{\mathrm{tr}} - M(\mathscr{D}_{\mathrm{tr}})\|^2 + \lambda \sum_{i=1,3,4} \|\mathbf{D}_{\mathrm{tr},(i)}\|_* \quad (5)$$

where $M(\cdot)$ applies the sampling mask of the subspace training data covering the sampled image contrast combinations, $\mathbf{D}_{\mathrm{tr},(i)}$ is the mode-i unfolding of $\mathscr{D}_{\mathrm{tr}}$, $\|\cdot\|_*$ denotes the nuclear norm, and λ weights the nuclear norm penalties. The core tensor $\mathscr{C}$ and the remaining temporal factor matrices can be quickly extracted from the completed $\widehat{\mathscr{D}}_{\mathrm{tr}}$ via the high-order SVD[47], and the temporal tensor $\mathscr{V}$ is then determined according to Eq. (4).

2.4.2 Spatial factor estimation—

The final stage estimates the spatial factor matrix $\mathbf{U}$ by fitting the temporal tensor $\mathscr{V}$ to the imaging data:

$$\mathbf{U} = \arg\min_{\mathbf{U}} \|\mathbf{d}_{\mathrm{img}} - \Omega(\mathbf{FS}(\mathscr{V} \times_1 \mathbf{U})\|^2 + R_s(\mathbf{U}) \quad (6)$$

where $\Omega(\cdot)$ is the undersampling operator, $\mathbf{F}$ applies spatial encoding, $\mathbf{S}$ applies multichannel encoding, and $R_s(\cdot)$ applies spatial TV regularization to leverage compressed sensing.

We specifically note that once the temporal tensor $\mathscr{V}$ has been estimated, Eq. (6) reduces to a subspace-constrained low-rank matrix recovery problem which combines the partial separability model[44] with additional regularization constraints as described by Zhao et al[48]. Similar subspace-constrained low-rank matrix imaging approaches have also been employed in many other different applications as well[49-51].

With $\mathbf{U}$ and $\mathscr{V}$, the complete image tensor is thus reconstructed according to Eq. (3), which can individually show the process of T1 recovery, T2 decay, and T1ρ decay along the respective time dimensions. An illustrative display of the image tensor is shown in Supporting Information Video S1.

2.5. Multiparametric mapping

After reconstructing the image tensor, voxel-wise multiparametric mapping can be performed following the signal equation:

$$S_n = A \cdot \frac{1 - e^{-\frac{TR}{T_1}}}{1 - e^{-\frac{TR}{T_1}}\cos(\alpha)} \left[1 + \left(Be^{-\frac{\tau}{T_2}} e^{-\frac{\tau_{\mathrm{SL}}}{\mathrm{T}_1\rho} - 1}\right)\left(e^{-\frac{TR}{T_1}}\cos(\alpha)\right)^n\right]\sin(\alpha) \quad (7)$$

where A absorbs proton density, overall B1 receive field, and T2* weighting, α denotes the FLASH flip angle, and B represents the effective inversion efficiency independent of T2 and T1ρ. We fit for A, B, T1, T2, T1ρ, and α (where fitting α accounts for the B1 effect on the FLASH pulse as well as the imperfect (i.e., nonrectangular) slab profile).

2.6. Imaging experiments

All imaging experiments were conducted on a 3T clinical scanner (Biograph mMR, Siemens Healthineers, Erlangen, Germany) using a 20-channel head coil.

2.6.1 Phantom study—An ISMRM/NIST phantom[52] (model 130, High Precision Devices, Boulder, Colorado) was scanned. Reference protocols for phantom study included inversion recovery spin echo (IR-SE) for T1 mapping, T2-weighted spin echo (T2-SE) for T2 mapping, and 3D T1ρ-prepared FLASH (T1ρ-FLASH) for T1ρ mapping. Scan parameters for Multitasking were: FOV=240x240mm^2, in-plane resolution=1.0x1.0mm^2, slice thickness=3.5mm. The detailed imaging protocol is in Supporting Information Table S1.

2.6.2 In vivo study—Healthy control and patient studies were approved by the institutional review board of Cedars-Sinai Medical Center. All subjects gave written informed consent before MRI. N=15 age-matched healthy volunteers (6 male, 9 female, age 44.7±15.1) without any brain diseases were recruited. Reference protocols included inversion recovery turbo spin echo (IR-TSE) for T1 mapping, T2-weighted multi-echo spin echo (ME-SE) for T2 mapping, and 3D T1ρ-FLASH for T1ρ mapping, with a total scan time of 25min. The whole-brain Multitasking sequence was applied twice to test the scan-rescan repeatability, with a scan time of 9min per scan. All scans used FOV=240 mm x 240 mm, in-plane resolution=1.0 mm x 1.0 mm, slice thickness=3.5 mm. The detailed imaging protocol is in Supporting Information Table S2. In addition, N=9 RRMS patients (1 male, 8 females, age 46.8±8.0, disease duration 11.5±7.9 years) who were referred by an MS specialist were enrolled for clinical validation. The Expanded Disability Status Scale (EDSS) for this patient cohort is 2.5±1.5. The Multitasking sequence was incorporated in a clinical MRI study and was run before any contrast agent administered as part of the clinical protocol.

2.7. Image analysis

All Multitasking image reconstructions were performed on a Linux workstation with a 2.70GHz dual 12-core Intel Xeon processor equipped with 256GB RAM and running MATLAB 2016b (MathWorks, Natick, Massachusetts). The reconstruction time was 0.8–1.5h for each subject. The penalty factor λ for weighting the nuclear norm in the tensor completion step was chosen based on the discrepancy principle[53]. The convex optimizations Eqs. (5) and (6) were solved via the alternating direction method of multipliers (ADMM) algorithm[54]. Specifically, the range restriction in Eq. (5) was implemented such that within each iteration, the variable update along the T1 relaxation dimension was conducted by projection onto the T1 relaxation subspace $\mathbf{W}$, while the variable update along other dimensions was conducted by soft-thresholding. This ensured that $\mathbf{D}_{\mathrm{tr},(2)}$ is contained within the T1 relaxation subspace, filling the empty T1 indices by interpolating according to the predetermined T1 subspace. The ranks for the spatial dimension (e.g., I) and for the T1 relaxation dimension (e.g., J) were determined from the –40dB threshold of the normalized singular value curves obtained from the SVD of the completed subspace training data and the training dictionary, respectively. The ranks for the T2 relaxation (i.e., K) and T1ρ

relaxation (i.e., L) dimensions were not truncated, as these dimensions were already penalized by the nuclear norm constraint in Eq. (5).

Voxel-wise quantitative T1/T2/T1ρ maps for all phantom and in vivo cases were obtained by fitting the reconstructed image tensor with Eq. (7). For controls and patients, four tissue compartments – white matter (WM), cortical gray matter (GM), putamen, and thalamus – were selected as regions of interest (ROIs) for data analysis. ROI segmentation was performed by thresholding on the raw reference/Multitasking images at approximately similar slice positions. We specifically note that for MS patients, focal WM lesions appeared hypointense on Multitasking images and thus could be ruled out from the WM ROI by proper thresholding. Cortical and deep GM lesions were not detectable with conventional MRI techniques including Multitasking and could not be ruled out from the corresponding ROIs. Example ROIs are shown in Supporting Information Figure S2 and Supporting Information Figure S3. Six synthetic qualitative contrast-weighted images were generated using the quantitative maps, where five of them are clinically adopted contrasts including T1-weighted MPRAGE (T1w), T2-weighted (T2w), proton-density-weighted (PDw), T2w-FLAIR, and double-inversion-recovery (DIR). We also synthesize a novel contrast, T1ρw-FLAIR, which is created by substituting T2 with T1ρ in the standard FLAIR signal model.

2.8. Quantitative analysis

For the phantom study, T1/T2/T1ρ values for each vial were calculated. Linear regression analysis was performed, and intraclass correlation coefficients (ICC) were calculated using IBM SPSS Statistics (Armonk, New York) with a two-way mixed model and 95% confidence level to evaluate the quantitative agreement between Multitasking and the reference.

For the healthy control study, measurement populations of T1/T2/T1ρ in the four tissue compartments were compared between Multitasking and the references. ICCs between Multitasking and the reference measurements were derived the same way as in the phantom study. Paired t-tests were performed to evaluate the significance between Multitasking and the reference measurements. The significance level was set as p=0.05. Scan-rescan repeatability was evaluated from the Bland-Altman and ICC analyses of the 1st and 2nd Multitasking scans. For each tissue compartment of each subject, the mean T1/T2/T1ρ values over the corresponding ROI was used to perform ICC, paired t-test, and Bland-Altman analyses.

For the patient study, measurement populations of T1/T2/T1ρ in the same four normal appearing (NA) tissue compartments were derived. For each measurement of each tissue, a one-way analysis of variance (ANOVA) was performed to evaluate the statistical significance between patients and healthy controls. The significance level was set as p=0.05. Receiver operating characteristic (ROC) curve analysis with binary logistic regression was performed using IBM SPSS Statistics to evaluate the accuracy in differentiating MS from healthy control based on either a single parameter (i.e., T1, T2, T1ρ) or the combination of three parameters (denoted as T1+T2+T1ρ), as measured by the area under the curve (AUC). A confidence interval (CI) of 95% was used. Measurements for all four tissue compartments were combined to calculate ROC curves.

3. Results

3.1. Phantom study

Multitasking T1/T2/T1ρ maps were generated with good image quality and SNR (Figure 2). Multitasking measurements and reference measurements showed excellent correlation with R^2=0.996, 0.999, and 0.998 for T1/T2/T1ρ respectively, as well as excellent agreement with ICC=0.998, 0.996, and 0.998 for T1/T2/T1ρ,respectively.

3.2. In vivo study

Simultaneously acquired Multitasking T1/T2/T1ρ maps were of high quality and comparable with reference maps, with well-preserved brain tissue structure and contrasts (Figure 3). Reference T1ρ maps appeared slightly blurry, presumably due to T1 contamination over the course of several readouts. Multitasking measurement distributions in each tissue compartment were: WM (T1:843.6±18.3; T2:75.9±2.8; T1ρ:82.7±3.2), GM (T1:1319.8±28.9; T2:83.9±3.6; T1ρ:90.9±3.0), putamen (T1:1110.3±43.3; T2:72.0±3.6; T1ρ:77.6±2.7), and thalamus (T1:1041.5±34.1; T2:76.0±3.5; T1ρ:83.7±3.8); Table 1 lists these in comparison to the references. Substantial quantitative agreement between Multitasking and the references was seen for T1/T2/T1ρ in all tissue compartments, with all ICC>0.81 within the “excellent” definition range[55] (Table 2). Small but statistically significant biases were seen between Multitasking and reference measurements: Multitasking T1 and T1ρ values were higher in all compartments (1.1%~9.0% higher for T1, and 2.0%~4.3% higher for T1ρ), while T2 values lower in all compartments (1.6%~3.3% lower). Despite the measurement biases, values of all tissue compartments were within the literature range[22,26,56-61] where available. No T1ρ literature values of putamen and thalamus were found.

Bland-Altman plots demonstrated good scan-rescan repeatability of Multitasking experiments for T1/T2/T1ρ measurements on all tissue compartments (Figure 4). For all subjects and tissue compartments, maximum T1, T2 and T1ρ variations were all less than 5%. All ICCs between the 1st and 2nd Multitasking sessions were >0.91, also indicating “excellent” agreement (Table 3).

Figure 5 showed example quantitative maps as well as synthetic and clinical weighted images of a 56-year-old female RRMS patient who had 20 years disease duration. The WM lesion was clearly delineated on Multitasking T1/T2/T1ρ maps (Figure 5A). Figure 5B demonstrated synthetic weighted images, where the lesion was clearly shown on T2w, T2w-FLAIR, T1ρw-FLAIR, and DIR. CSF was nulled on T2w-FLAIR, T1ρw-FLAIR, and DIR, yielding better visualization of lesion than other synthetic contrast-weighted images. It appeared that the lesion is most conspicuous on T1ρw-FLAIR and DIR. T1w and T2w-FLAIR were the only available corresponding clinical images with which the corresponding synthetic ones were comparable (Figure 5C).

Table 4 showed population statistics for Multitasking measurements in RRMS patients and the results of comparisons against healthy controls. We found significant differences for T1 in NAWM (900.1±13.0, p=3.9x10^{-7}) compared to healthy controls. T2 was also significantly higher in NAWM of patients (78.7±1.9, p=0.019). Significantly higher T1ρ was

observed in all four compartments: NAWM (86.9±2.5, p=0.005), NAGM (95.8±3.0, p=0.001), putamen (80.5±2.1, p=0.016), and thalamus (86.5±2.5, p=0.024).

ROC analysis (Figure 6) showed that when using a single parameter, T1ρ had the highest AUC point estimate for discriminating MS with healthy control with AUC=0.831 (95%CI: 0.744-0.918), followed by T1 with AUC=0.807 (95%CI: 0.714-0.900) and T2 with AUC=0.686 (95%CI: 0.574-0.797). The combination of all three parameters had significantly higher accuracy than any individual parameter, with AUC=0.972 (95%CI: 0.944-0.999).

4. Discussion

We extended the existing MR Multitasking technique to achieve simultaneous quantification of T1/T2/T1ρ with whole-brain coverage in a clinically feasible scan time. By modeling the underlying image as a multidimensional tensor, characterizing each relaxation process as a different time dimension, and exploiting the strong spatiotemporal correlations along and across dimensions, this framework is capable of accelerating the imaging session, thus producing an efficient MR exam in clinical settings.

Simultaneous multiparametric mapping approaches have been widely explored in recent years, as they have several significant merits: i) production of quantitative information rarely available in conventional clinical MR exams, which has the potential to have higher sensitivity, specificity, and reproducibility beneficial to inter-subject or inter-site comparison, longitudinal follow-up, and detection of biological tissue changes; ii) production of quantitative biomarkers that allow comprehensive measurement of tissue properties under various diseases; and iii) substantial acceleration compared to conventional quantitative MRI methods which are usually performed in separate scans, leading to shortened MR sessions, co-registered measurements, and significantly reduced motion artifacts. Popular approaches that quantify proton density, T1, T2, T2*, ADC, and perfusion and vascular permeability parameters have been proposed and drawn extensive interests, using MR fingerprinting, MR Multitasking, and more[28,30,32,33,46,62-64]. As an emerging contrast mechanism specially characterizing low-frequency biochemical motional process, T1ρ has yet to be fully explored, while the acquisition can be extremely inefficient (10-20min) especially when whole anatomical coverage is desired[65-68]. Furthermore, with such a long scan time, clinical scans could be prone to motion artifacts. This work quantifies whole-brain T1ρ along with T1 and T2 simultaneously in 9min which is significantly shorter than separate reference T1/T2/T1ρ acquisition performed in 25min in this study, thus being promising for clinical research.

The proposed method produced high quality and co-registered multiparametric maps and T1/T2/T1ρ measurements in the phantom and brain tissue compartments with substantial quantitative agreement with reference measurements. Significantly different measurement biases were seen between Multitasking and the reference methods, which may be due to several factors. Firstly, the T1 differences could be related to both preparation scheme differences (IR vs. T2-IR/T1ρ-IR) and readout differences (TSE vs. FLASH). Besides, it has been shown that IR-TSE could lead to T1 underestimation in the brain compared to the

traditional “gold standard” IR-SE[28]. Secondly, T2-preparations might lead to T2 underestimation due to B1 inhomogeneities[33,69], while ME-SE was likely to cause T2 overestimation due to stimulated echo contamination[70]. Lastly, reference T1ρ mapping was subject to T1 contamination during the FLASH readouts despite the implementation of 2-shot acquisition to allow fewer phase encoding lines per shot, which could also be the reason of blurriness in reference T1ρ maps but could be improved in future works by either implementing centric readout mode in both phase and partition encoding directions or using more shots at the expense of a longer scan time. We also note two other factors that may influence the accuracy of the relaxation parameters in Multitasking and the references. One factor is the magnetization transfer (MT) effect through dipolar coupling and chemical exchange within myelinated brain tissues[71], which alters the shape of the inversion recovery curves following the inversion pulse of IR-TSE and the saturation pulse (i.e., the second 90° tip-down) of T2-IR/T1ρ-IR in different manners, causing a shorter apparent T1 to different extents[72]. Furthermore, the MT effect may lead to T2 underestimation in ME-SE due to the saturation of the macromolecules through the use of high-power RF pulses in echo trains[73]. The other factor is the multicomponent nature of T2 and T1ρ due to the complexity of heterogeneous tissue structures composed of different pools[66,74-77], where each component describes a unique relaxation process that can be associated with residual dipolar interactions, chemical exchange, free pool or bound pool in a distinct tissue compartment. In this work, we adopted the conventional single component model for T2 and T1ρ in Multitasking and reference T2/T1ρ mapping for scan time consideration. However, multicomponent modeling could be easily carried out with Multitasking with more T2-IR/T1ρ-IR pulses.

Here, the Tucker form of tensor decomposition was employed to implement the LRT image model. However, we note that various tensor decomposition methods are available, such as canonical decomposition[38]. A major advantage of Tucker decomposition over canonical decomposition is that Tucker decomposition allows the control over the rank of each dimension, therefore optimizing the signal compression along each dimension, while canonical decomposition enforces a single rank to model all the dynamics which could result in less compression and higher memory usage. As a rule of thumb, Tucker decomposition is recommended for subspace estimation and signal compression[78]. Other tensor decomposition methods are beyond the scope of the discussion and are comprehensively reviewed in Reference 38.

Six synthetic contrast-weighted images along with three quantitative maps were generated with the proposed technique, which in the future have the potential to replace conventional qualitative scans in the clinical workflow. Future work will compare the diagnostic accuracy of the synthetic and clinical images as further validation. In the results of this study, the MS lesion was conspicuous on all three parametric maps, while the lesion on T1ρ map and synthetic T1ρw-FLAIR appeared more prominent than on T2 map and synthetic T2w-FLAIR. This is qualitatively consistent with the findings reported in a previous study, where T1ρ showed better lesion CNR than T2[26]. T1-based synthetic DIR also provided excellent visualization of lesion. However, whether T1 or T1ρ is better in terms of lesion characterization and diagnostic values needs further investigation. T1w, T2w, and PDw

appeared to have less diagnostic value compared to the other three synthetic images in terms of small lesions in MS, but could still be important in other neurological diseases.

In this work, significantly higher T1/T2/T1ρ values in NAWM of RRMS patients were observed compared to healthy controls, which was consistent with previous findings[26,27,79,80]. Such differences could indicate the presence of myelin content reduction, axonal degeneration, inflammatory reaction, and the accumulation of extracellular water suggestive of blood brain barrier leakage in NAWM[81,82]. No significant differences were observed for T1/T2 values in NAGM, putamen, and thalamus. Although cortical and deep GM pathologies such as demyelinating lesions are also prominent in MS, they are typically less detected with conventional MRI techniques due to low myelin densities and reduced number of axons in GM cellular matrices, and inflammation of GM is less pronounced than WM during progressive stages of MS and could involve more subtle tissue alterations[83,84]. On the other hand, significantly higher T1ρ values were observed in both NAGM and NA deep GM (i.e., putamen, thalamus) regions of RRMS patients compared to healthy controls, suggesting that T1ρ could be more sensitive to cortical and deep GM demyelination than T1 and T2. A potential reason is that low-frequency protein infiltration and chemical exchanges could be associated with GM demyelination and neuronal loss which could be more detectable with T1ρ than T1 and T2. Brain biopsies at early stage of MS demonstrated substantial prevalence of perivascular CD3+ and CD8+ T-cell infiltrates in demyelinating cortical lesions[85]. Besides, T1ρ is known to be sensitive to a broader range of spin dynamics and has been shown to be a sensitive indicator of neuronal cell loss in neurological disorders[86]. Interestingly, two previous studies, Gonyea et al.[26] and Mangia et al.[27], reported nonsignificant differences of T1ρ in NAGM between RRMS and healthy controls. There are several potential reasons for this. First, these preliminary studies, including ours, have relatively small sample size (N=13 healthy controls and N=9 RRMS patients in our study; N=24 healthy controls and N=13 RRMS patients in Gonyea et al.; N=7 healthy controls and N=9 RRMS patients in Mangia et al.); if a small difference indeed exists, then reduced statistical power would result in a significant difference being found only in a subset of studies. Further clinical validations with larger cohorts would be desirable to provide sufficient statistical power to resolve any disparities. Second, compared to the patient demographics in Gonyea et al., the patients recruited for our study had longer disease duration (11.5 vs. 7.8 years) and higher EDSS (2.5 vs. 1.8), which indicated longer disease progression and more severe disability. As a result, our patients were likely to experience further pathologies (e.g., demyelination, inflammatory reaction) that could potentially be detectable with T1ρ. Third, Mangia et al. had similar patient demographics as our study, but employed a single slice adiabatic T1ρ pulse sequence with adiabatic full passage hyperbolic secant pulse train on a 4T scanner, which was not widely available for clinical practices and had very different T1ρ physics intrinsically under a train of adiabatic pulses[87,88], with substantially different T1ρ measurements (172ms T1ρ of WM and 221ms T1ρ of GM in control, and 182ms T1ρ of NAWM and 225ms T1ρ of NAGM in RRMS patients) than ours and literature ranges at 3T. However, we do note that due to limited studies available, the precise mechanisms of T1ρ in MS are still not clear. Optimal magnetic field strength and T1ρ pulse sequence, as well as the effectiveness of T1ρ dispersion (i.e., the relationship

between T1ρ relaxation time and spin-lock frequency) for MS tissue characterization also requires further investigation.

The ROC analysis in our study suggested that quantitative T1/T2/T1ρ relaxation times in NAWM, NAGM, and NA deep GM were feasible for MS tissue characterization and discrimination between healthy controls. T1ρ had better discriminating power than T1 and T2, and the combination of T1/T2/T1ρ had better discriminating power than using either single parameter alone. Demyelination and axonal loss across various brain regions are prevalent at very early stages of MS. Our results indicated that the combination of T1/T2/T1ρ could offer complementary tissue information and perhaps have potential to allow early recognition of inflammatory process and aid early diagnosis on high risk patients. Moreover, various combination of relaxation parameters could potentially improve the prediction of cognitive performance, fatigue, and disability by correlating with clinical cognitive and behavioral test scores[89]. In addition, the combination of T1/T2/T1ρ could also act as tissue biomarkers for the treatment monitoring of MS, as the changes in relaxation times of normal appearing brain tissues could indicate repair mechanisms (e.g., remyelination, increased axonal densities) in the brain[6]. These aspects would significantly improve the clinical outcome and patient care.

One major limitation of this work is that we have yet to achieve ≤1.0mm slice resolution in a reasonable scan time, which is a common practice in MS imaging. The current 3.5mm slice thickness may lead to missed detection of small lesions, or inaccurate lesion characterization due to partial volume effects. Future technical improvement will focus on shortening the scan time for higher-resolution imaging, for example by deep-learning super-resolution in the slice direction[90,91]. We also note the limitation of our phantom study with respect to the suitability for T1ρ measurements, as the NIST phantom has a simple structure and doesn't exhibit protein and chemical exchange processes. This could be improved using phantom solutions with different agarose concentration[36,37]. Lastly, we have yet to demonstrate the feasibility under different types of head motion. In this work, motion is mitigated by head fixation using padding and cushions for all in vivo scans. However, it is fundamentally feasible to handle motion in the general Multitasking framework, either by identification of motion-corrupted data followed by subsequent removal[33,46], or by motion-resolved imaging which models motion as a separate time dimension in the LRT framework[32,34]. A detailed investigation involving both in-plane and through-plane motion will be conducted in a separate work.

5. Conclusion

Three-dimensional, whole-brain simultaneous T1/T2/T1ρ quantification is achieved in 9min with MR Multitasking. This novel technique produces T1/T2/T1ρ values in substantial quantitative agreement with reference methods, demonstrates excellent scan-rescan repeatability, and provides synthetic contrast-weighted images mimicking clinical images in addition to the three quantitative maps. The combination of T1/T2/T1ρ in normal appearing WM, cortical GM, and deep GM regions better discriminates MS patients from healthy controls as compared to using a single measurement alone, having the potential for early diagnosis and monitoring treatment response in MS. Future work will focus on achieving

higher slice resolution, dealing with motion, and comprehensive clinical studies with larger cohorts.

Supplementary Material

Refer to Web version on PubMed Central for supplementary material.

Acknowledgements

This work was supported by NIH 1R01EB028146. Anthony G. Christodoulou and Debiao Li contributed equally to this work.

References

1. Badve C, Yu A, Dastmalchian S, et al. MR Fingerprinting of Adult Brain Tumors: Initial Experience. AJNR Am J Neuroradiol. 2017;38(3):492–499. [PubMed: 28034994]
2. Hattingen E, Jurcoane A, Daneshvar K, et al. Quantitative T2 mapping of recurrent glioblastoma under bevacizumab improves monitoring for non-enhancing tumor progression and predicts overall survival. Neuro Oncol. 2013;15(10):1395–1404. [PubMed: 23925453]
3. Lescher S, Jurcoane A, Veit A, Bahr O, Deichmann R, Hattingen E. Quantitative T1 and T2 mapping in recurrent glioblastomas under bevacizumab: earlier detection of tumor progression compared to conventional MRI. Neuroradiology. 2015;57(1):11–20. [PubMed: 25287076]
4. Muller A, Jurcoane A, Kebir S, et al. Quantitative T1-mapping detects cloudy-enhancing tumor compartments predicting outcome of patients with glioblastoma. Cancer Med. 2017;6(1):89–99. [PubMed: 27891815]
5. Blystad I, Hakansson I, Tisell A, et al. Quantitative MRI for Analysis of Active Multiple Sclerosis Lesions without Gadolinium-Based Contrast Agent. AJNR Am J Neuroradiol. 2016;37(1):94–100. [PubMed: 26471751]
6. Bonnier G, Marechal B, Fartaria MJ, et al. The Combined Quantification and Interpretation of Multiple Quantitative Magnetic Resonance Imaging Metrics Enlightens Longitudinal Changes Compatible with Brain Repair in Relapsing-Remitting Multiple Sclerosis Patients. Front Neurol. 2017;8:506. [PubMed: 29021778]
7. Manfredonia F, Ciccarelli O, Khaleeli Z, et al. Normal-appearing brain t1 relaxation time predicts disability in early primary progressive multiple sclerosis. Arch Neurol. 2007;64(3):411–415. [PubMed: 17353385]
8. Tardif CL, Bedell BJ, Eskildsen SF, Collins DL, Pike GB. Quantitative magnetic resonance imaging of cortical multiple sclerosis pathology. Mult Scler Int. 2012;2012:742018. [PubMed: 23213531]
9. Vrenken H, Rombouts SA, Pouwels PJ, Barkhof F. Voxel-based analysis of quantitative T1 maps demonstrates that multiple sclerosis acts throughout the normal-appearing white matter. AJNR Am J Neuroradiol. 2006;27(4):868–874. [PubMed: 16611780]
10. Bartzokis G, Cummings JL, Sultzer D, Henderson VW, Nuechterlein KH, Mintz J. White matter structural integrity in healthy aging adults and patients with Alzheimer disease: a magnetic resonance imaging study. Arch Neurol. 2003;60(3):393–398. [PubMed: 12633151]
11. Knight MJ, McCann B, Tsivos D, Dillon S, Coulthard E, Kauppinen RA. Quantitative T2 mapping of white matter: applications for ageing and cognitive decline. Phys Med Biol. 2016;61(15):5587–5605. [PubMed: 27384985]
12. Luo Z, Zhuang X, Kumar D, et al. The correlation of hippocampal T2-mapping with neuropsychology test in patients with Alzheimer's disease. PLoS One. 2013;8(9):e76203. [PubMed: 24098779]
13. Baudrexel S, Nurnberger L, Rub U, et al. Quantitative mapping of T1 and T2* discloses nigral and brainstem pathology in early Parkinson's disease. Neuroimage. 2010;51(2):512–520. [PubMed: 20211271]

14. Focke NK, Helms G, Pantel PM, et al. Differentiation of typical and atypical Parkinson syndromes by quantitative MR imaging. AJNR Am J Neuroradiol. 2011;32(11):2087–2092. [PubMed: 21998102]
15. Vymazal J, Righini A, Brooks RA, et al. T1 and T2 in the brain of healthy subjects, patients with Parkinson disease, and patients with multiple system atrophy: relation to iron content. Radiology. 1999;211(2):489–495. [PubMed: 10228533]
16. Wang YX, Zhang Q, Li X, Chen W, Ahuja A, Yuan J. T1rho magnetic resonance: basic physics principles and applications in knee and intervertebral disc imaging. Quant Imaging Med Surg. 2015;5(6):858–885. [PubMed: 26807369]
17. Le J, Peng Q, Sperling K. Biochemical magnetic resonance imaging of knee articular cartilage: T1rho and T2 mapping as cartilage degeneration biomarkers. Ann N Y Acad Sci. 2016;1383(1):34–42. [PubMed: 27472534]
18. Li X, Benjamin Ma C, Link TM, et al. In vivo T(1rho) and T(2) mapping of articular cartilage in osteoarthritis of the knee using 3 T MRI. Osteoarthritis Cartilage. 2007;15(7):789–797. [PubMed: 17307365]
19. Stahl R, Luke A, Li X, et al. T1rho, T2 and focal knee cartilage abnormalities in physically active and sedentary healthy subjects versus early OA patients--a 3.0-Tesla MRI study. Eur Radiol. 2009;19(1):132–143. [PubMed: 18709373]
20. Witschey WR, Borthakur A, Fenty M, et al. T1rho MRI quantification of arthroscopically confirmed cartilage degeneration. Magn Reson Med. 2010;63(5):1376–1382. [PubMed: 20432308]
21. Borthakur A, Sochor M, Davatzikos C, Trojanowski JQ, Clark CM. T1rho MRI of Alzheimer's disease. Neuroimage. 2008;41(4):1199–1205. [PubMed: 18479942]
22. Haris M, Yadav SK, Rizwan A, et al. T1rho MRI and CSF biomarkers in diagnosis of Alzheimer's disease. Neuroimage Clin. 2015;7:598–604. [PubMed: 25844314]
23. Haris M, Singh A, Cai K, et al. T1rho (T1rho) MR imaging in Alzheimer's disease and Parkinson's disease with and without dementia. J Neurol. 2011;258(3):380–385. [PubMed: 20924593]
24. Nestrasil I, Michaeli S, Liimatainen T, et al. T1rho and T2rho MRI in the evaluation of Parkinson's disease. J Neurol. 2010;257(6):964–968. [PubMed: 20058018]
25. Jokivarsi KT, Hiltunen Y, Grohn H, Tuunanen P, Grohn OH, Kauppinen RA. Estimation of the onset time of cerebral ischemia using T1rho and T2 MRI in rats. Stroke. 2010;41(10):2335–2340. [PubMed: 20814006]
26. Gonyea JV, Watts R, Applebee A, et al. In vivo quantitative whole-brain T1 rho MRI of multiple sclerosis. J Magn Reson Imaging. 2015;42(6):1623–1630. [PubMed: 26032694]
27. Mangia S, Carpenter AF, Tyan AE, Eberly LE, Garwood M, Michaeli S. Magnetization transfer and adiabatic T1rho MRI reveal abnormalities in normal-appearing white matter of subjects with multiple sclerosis. Mult Scler. 2014;20(8):1066–1073. [PubMed: 24336350]
28. Deoni SC, Rutt BK, Peters TM. Rapid combined T1 and T2 mapping using gradient recalled acquisition in the steady state. Magn Reson Med. 2003;49(3):515–526. [PubMed: 12594755]
29. Chen Y, Panda A, Pahwa S, et al. Three-dimensional MR Fingerprinting for Quantitative Breast Imaging. Radiology. 2019;290(1):33–40. [PubMed: 30375925]
30. Ma D, Gulani V, Seiberlich N, et al. Magnetic resonance fingerprinting. Nature. 2013;495(7440):187–192. [PubMed: 23486058]
31. Yu AC, Badve C, Ponsky LE, et al. Development of a Combined MR Fingerprinting and Diffusion Examination for Prostate Cancer. Radiology. 2017;283(3):729–738. [PubMed: 28187264]
32. Christodoulou AG, Shaw JL, Nguyen C, et al. Magnetic resonance multitasking for motion-resolved quantitative cardiovascular imaging. Nat Biomed Eng. 2018;2(4):215–226. [PubMed: 30237910]
33. Ma S, Nguyen CT, Han F, et al. Three-dimensional simultaneous brain T1 , T2 , and ADC mapping with MR Multitasking. Magn Reson Med. 2020;84(1):72–88. [PubMed: 31765496]
34. Shaw JL, Yang Q, Zhou Z, et al. Free-breathing, non-ECG, continuous myocardial T1 mapping with cardiovascular magnetic resonance multitasking. Magn Reson Med. 2019;81(4):2450–2463. [PubMed: 30450749]

35. Li X, Wyatt C, Rivoire J, et al. Simultaneous acquisition of T1rho and T2 quantification in knee cartilage: repeatability and diurnal variation. J Magn Reson Imaging. 2014;39(5):1287–1293. [PubMed: 23897756]
36. Wyatt CR, Barbara TM, Guimaraes AR. T1rho magnetic resonance fingerprinting. NMR Biomed. 2020;33(5):e4284. [PubMed: 32125050]
37. Sharafi A, Zibetti MVW, Chang G, Cloos M, Regatte RR. MR fingerprinting for rapid simultaneous T1 , T2 , and T1 rho relaxation mapping of the human articular cartilage at 3T. Magn Reson Med. 2020.
38. Kolda TG, Bader BW. Tensor Decompositions and Applications. Siam Rev. 2009;51(3):455–500.
39. Nezafat R, Stuber M, Ouwerkerk R, Gharib AM, Desai MY, Pettigrew RI. B1-insensitive T2 preparation for improved coronary magnetic resonance angiography at 3 T. Magn Reson Med. 2006;55(4):858–864. [PubMed: 16538606]
40. Brown R, Nguyen TD, Spincemaille P, et al. Effect of blood flow on double inversion recovery vessel wall MRI of the peripheral arteries: quantitation with T2 mapping and comparison with flow-insensitive T2-prepared inversion recovery imaging. Magn Reson Med. 2010;63(3):736–744. [PubMed: 20187182]
41. Mitrea BG, Krafft AJ, Song R, Loeffler RB, Hillenbrand CM. Paired self-compensated spin-lock preparation for improved T1rho quantification. J Magn Reson. 2016;268:49–57. [PubMed: 27161095]
42. Witschey WR 2nd, Borthakur A, Elliott MA, et al. Artifacts in T1 rho-weighted imaging: compensation for B(1) and B(0) field imperfections. J Magn Reson. 2007;186(1):75–85. [PubMed: 17291799]
43. He J, Liu Q, Christodoulou A, Ma C, Lam F, Liang Z-P. Accelerated high-dimensional MR imaging with sparse sampling using low-rank tensors. IEEE Trans Med Imaging. 2016;35(9):2119–2129. [PubMed: 27093543]
44. Liang Z-P. Spatiotemporal imagingwith partially separable functions. *In* Proceedings of the 4th IEEE International Symposium on Biomedical Imaging: From Nano to Macro, Arlington, Virginia, USA, 2007. p. 988–991.
45. Tucker LR. Some mathematical notes on three-mode factor analysis. Psychometrika. 1966;31(3):279–311. [PubMed: 5221127]
46. Wang N, Christodoulou AG, Xie Y, et al. Quantitative 3D dynamic contrast-enhanced (DCE) MR imaging of carotid vessel wall by fast T1 mapping using Multitasking. Magn Reson Med. 2019;81(4):2302–2314. [PubMed: 30368891]
47. De Lathauwer L, De Moor B, Vandewalle J. A multilinear singular value decomposition. Siam J Matrix Anal A. 2000;21(4):1253–1278.
48. Zhao B, Haldar JP, Christodoulou AG, Liang ZP. Image reconstruction from highly undersampled (k, t)-space data with joint partial separability and sparsity constraints. IEEE Trans Med Imaging. 2012;31(9):1809–1820. [PubMed: 22695345]
49. Huang C, Graff CG, Clarkson EW, Bilgin A, Altbach MI. T2 mapping from highly undersampled data by reconstruction of principal component coefficient maps using compressed sensing. Magn Reson Med. 2012;67(5):1355–1366. [PubMed: 22190358]
50. Tamir JI, Uecker M, Chen W, et al. T2 shuffling: Sharp, multicontrast, volumetric fast spin-echo imaging. Magn Reson Med. 2017;77(1):180–195. [PubMed: 26786745]
51. Zhao B, Lu W, Hitchens TK, Lam F, Ho C, Liang ZP. Accelerated MR parameter mapping with low-rank and sparsity constraints. Magn Reson Med. 2015;74(2):489–498. [PubMed: 25163720]
52. Russek SE BM, Jackson EF, Jennings DL, Evelhoch JL, Gunter JL, Sorensen AG. Characterization of NIST/ISMRM MRI System Phantom. *In* Proceedings of the 20th Annual Meeting of ISMRM, Melbourne, Australia, 2012. Abstract 2456.
53. Morozov VA. On the solution of functional equations by the method of regularization. Soviet Math Dokl. 1966; 7:414–417.
54. Boyd S, Parikh N, Chu E, Peleato B, Eckstein J. Distributed optimization and statistical learning via the alternating direction method of multipliers. Foundations and Trends® in Machine Learning. 2011;3(1):1–122.

55. Cicchetti DV. Guidelines, criteria, and rules of thumb for evaluating normed and standardized assessment instruments in psychology. Psychological assessment. 1994;6(4):284.
56. Borthakur A, Wheaton AJ, Gougoutas AJ, et al. In vivo measurement of T1rho dispersion in the human brain at 1.5 tesla. J Magn Reson Imaging. 2004;19(4):403–409. [PubMed: 15065163]
57. Kumar R, Delshad S, Macey PM, Woo MA, Harper RM. Development of T2-relaxation values in regional brain sites during adolescence. Magn Reson Imaging. 2011;29(2):185–193. [PubMed: 20933351]
58. Ma D, Jiang Y, Chen Y, et al. Fast 3D magnetic resonance fingerprinting for a whole-brain coverage. Magn Reson Med. 2018;79(4):2190–2197. [PubMed: 28833436]
59. Okubo G, Okada T, Yamamoto A, et al. Relationship between aging and T1 relaxation time in deep gray matter: A voxel-based analysis. J Magn Reson Imaging. 2017;46(3):724–731. [PubMed: 28152255]
60. Stanisz GJ, Odrobina EE, Pun J, et al. T1, T2 relaxation and magnetization transfer in tissue at 3T. Magn Reson Med. 2005;54(3):507–512. [PubMed: 16086319]
61. Wansapura JP, Holland SK, Dunn RS, Ball WS Jr. NMR relaxation times in the human brain at 3.0 tesla. J Magn Reson Imaging. 1999;9(4):531–538. [PubMed: 10232510]
62. Gras V, Farrher E, Grinberg F, Shah NJ. Diffusion-weighted DESS protocol optimization for simultaneous mapping of the mean diffusivity, proton density and relaxation times at 3 Tesla. Magn Reson Med. 2017;78(1):130–141. [PubMed: 27476684]
63. Hutter J, Slator PJ, Christiaens D, et al. Integrated and efficient diffusion-relaxometry using ZEBRA. Sci Rep. 2018;8(1):15138. [PubMed: 30310108]
64. Wyatt CR, Smith TB, Sammi MK, Rooney WD, Guimaraes AR. Multi-parametric T2 * magnetic resonance fingerprinting using variable echo times. NMR Biomed. 2018;31(9):e3951. [PubMed: 30011109]
65. Iyer SK, Moon B, Hwuang E, et al. Accelerated free-breathing 3D T1 cardiovascular magnetic resonance using multicoil compressed sensing. Journal of Cardiovascular Magnetic Resonance. 2019;21.
66. Menon RG, Sharafi A, Windschuh J, Regatte RR. Bi-exponential 3D-T1rho mapping of whole brain at 3 T. Sci Rep. 2018;8(1):1176. [PubMed: 29352234]
67. Sharafi A, Xia D, Chang G, Regatte RR. Biexponential T1rho relaxation mapping of human knee cartilage in vivo at 3 T. NMR Biomed. 2017;30(10).
68. Witschey WR, Borthakur A, Elliott MA, et al. T1rho-prepared balanced gradient echo for rapid 3D T1rho MRI. J Magn Reson Imaging. 2008;28(3):744–754. [PubMed: 18777535]
69. Jiang Y, Ma D, Keenan KE, Stupic KF, Gulani V, Griswold MA. Repeatability of magnetic resonance fingerprinting T1 and T2 estimates assessed using the ISMRM/NIST MRI system phantom. Magn Reson Med. 2017;78(4):1452–1457. [PubMed: 27790751]
70. McPhee KC, Wilman AH. Limitations of skipping echoes for exponential T2 fitting. J Magn Reson Imaging. 2018;48(5):1432–1440. [PubMed: 29687931]
71. van Gelderen P, Jiang X, Duyn JH. Effects of magnetization transfer on T1 contrast in human brain white matter. Neuroimage. 2016;128:85–95. [PubMed: 26724780]
72. Kellman P, Hansen MS. T1-mapping in the heart: accuracy and precision. J Cardiovasc Magn Reson. 2014;16:2. [PubMed: 24387626]
73. Radunsky D, Blumenfeld-Katzir T, Volovyk O, et al. Analysis of magnetization transfer (MT) influence on quantitative mapping of T2 relaxation time. Magn Reson Med. 2019;82(1):145–158. [PubMed: 30860287]
74. Oh J, Han ET, Pelletier D, Nelson SJ. Measurement of in vivo multi-component T2 relaxation times for brain tissue using multi-slice T2 prep at 1.5 and 3 T. Magn Reson Imaging. 2006;24(1):33–43. [PubMed: 16410176]
75. Reiter DA, Lin PC, Fishbein KW, Spencer RG. Multicomponent T2 relaxation analysis in cartilage. Magn Reson Med. 2009;61(4):803–809. [PubMed: 19189393]
76. Zibetti MVW, Helou ES, Sharafi A, Regatte RR. Fast multicomponent 3D-T1rho relaxometry. NMR Biomed. 2020:e4318. [PubMed: 32359000]

77. Kim D, Wisnowski JL, Nguyen CT, Haldar JP. Multidimensional correlation spectroscopic imaging of exponential decays: From theoretical principles to in vivo human applications. NMR Biomed. 2020:e4244. [PubMed: 31909534]

78. Rabanser S, Shchur O, Günnemann S. Introduction to tensor decompositions and their applications in machine learning. arXiv preprint arXiv:171110781. 2017.

79. Neema M, Goldberg-Zimring D, Guss ZD, et al. 3 T MRI relaxometry detects T2 prolongation in the cerebral normal-appearing white matter in multiple sclerosis. Neuroimage. 2009;46(3):633–641. [PubMed: 19281850]

80. Vrenken H, Geurts JJ, Knol DL, et al. Whole-brain T1 mapping in multiple sclerosis: global changes of normal-appearing gray and white matter. Radiology. 2006;240(3):811–820. [PubMed: 16868279]

81. Lassmann H Multiple Sclerosis Pathology. Cold Spring Harb Perspect Med. 2018;8(3).

82. Plumb J, McQuaid S, Mirakhur M, Kirk J. Abnormal endothelial tight junctions in active lesions and normal-appearing white matter in multiple sclerosis. Brain Pathol. 2002;12(2):154–169. [PubMed: 11958369]

83. Hulst HE, Geurts JJ. Gray matter imaging in multiple sclerosis: what have we learned? BMC Neurol. 2011;11:153. [PubMed: 22152037]

84. Klaver R, De Vries HE, Schenk GJ, Geurts JJ. Grey matter damage in multiple sclerosis: a pathology perspective. Prion. 2013;7(1):66–75. [PubMed: 23324595]

85. Lucchinetti CF, Popescu BF, Bunyan RF, et al. Inflammatory cortical demyelination in early multiple sclerosis. N Engl J Med. 2011;365(23):2188–2197. [PubMed: 22150037]

86. Michaeli S, Oz G, Sorce DJ, et al. Assessment of brain iron and neuronal integrity in patients with Parkinson's disease using novel MRI contrasts. Mov Disord. 2007;22(3):334–340. [PubMed: 17149719]

87. Mangia S, Liimatainen T, Garwood M, Michaeli S. Rotating frame relaxation during adiabatic pulses vs. conventional spin lock: simulations and experimental results at 4 T. Magn Reson Imaging. 2009;27(8):1074–1087. [PubMed: 19559559]

88. Michaeli S, Sorce DJ, Springer CS Jr., Ugurbil K, Garwood M. T1rho MRI contrast in the human brain: modulation of the longitudinal rotating frame relaxation shutter-speed during an adiabatic RF pulse. J Magn Reson. 2006;181(1):135–147. [PubMed: 16675277]

89. Bonnier G, Roche A, Romascano D, et al. Advanced MRI unravels the nature of tissue alterations in early multiple sclerosis. Ann Clin Transl Neurol. 2014;1(6):423–432. [PubMed: 25356412]

90. Pham CH, Tor-Diez C, Meunier H, et al. Multiscale brain MRI super-resolution using deep 3D convolutional networks. Comput Med Imaging Graph. 2019;77:101647. [PubMed: 31493703]

91. Chen Y, Shi F, Christodoulou AG, Xie Y, Zhou Z, Li D. Efficient and accurate MRI super-resolution using a generative adversarial network and 3D multi-level densely connected network. In: International conference on medical image computing and computer-assisted intervention. Springer, Berlin, 2018. pp 91–99.

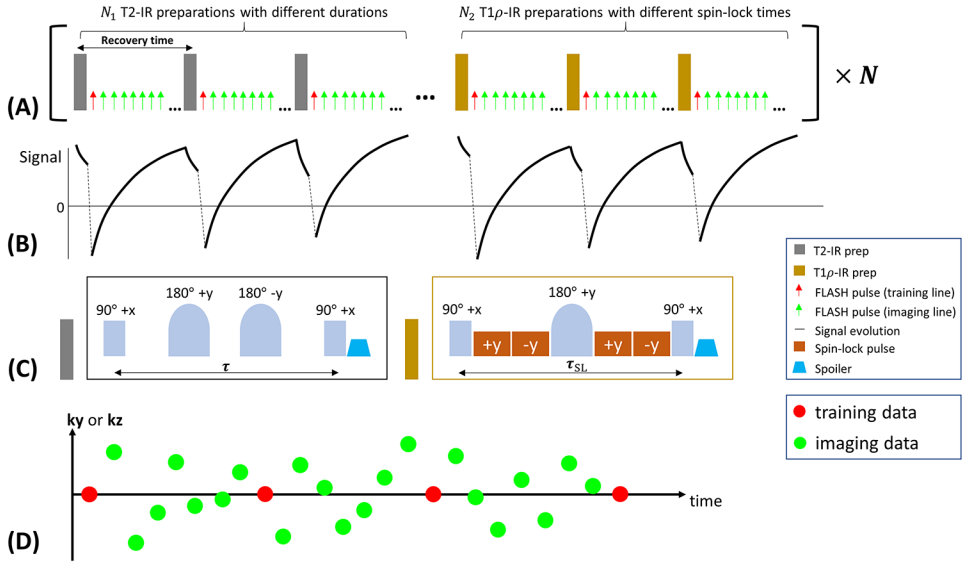

Figure 1.

(A) General sequence structure with interleaved T2-IR pulses and T1ρ-IR pulses. 3D FLASH readouts fill the entire recovery period. (B) Demonstration of signal evolution. The signal follows an exponential decay during the preparations and follows a look-locker inversion recovery during FLASH readouts. (C) Construction of T2-IR preparation pulses and T1ρ-IR preparation pulses, where T2-IR uses BIREF adiabatic refocusing pulses in an MLEV phase pair scheme and T1ρ-IR uses a paired self-compensated scheme. (D) K-space sampling demonstration. Imaging data are sampled from the entire k-space with Gaussian density. Training data periodically samples the center k-space line every 8 readouts.

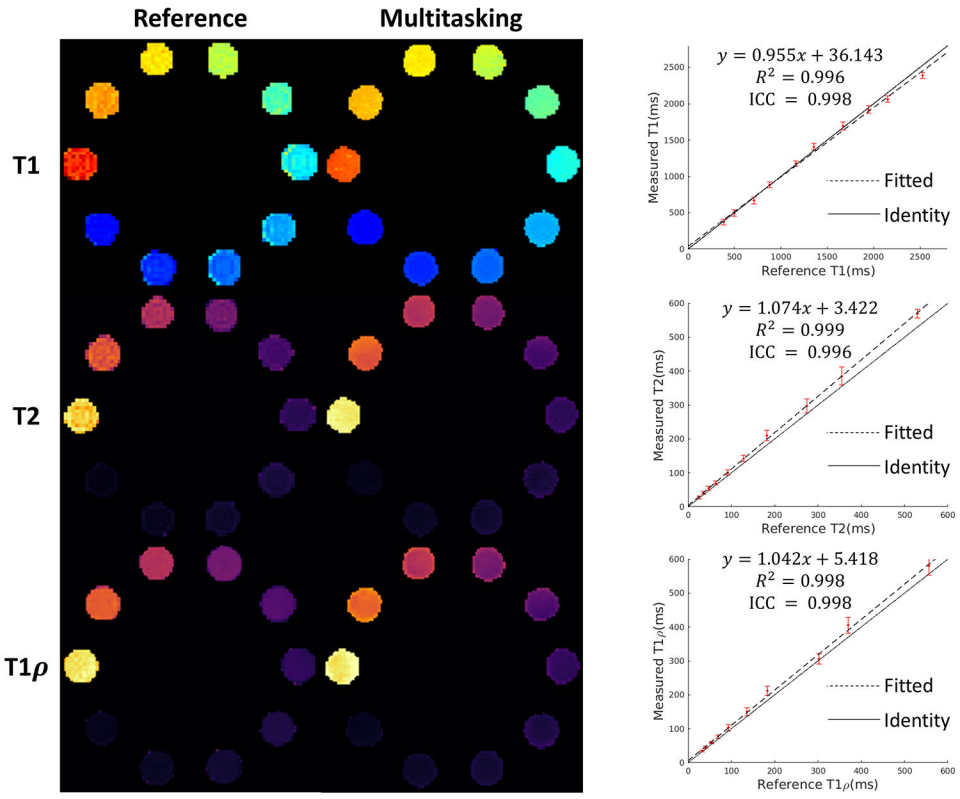

Figure 2.

Phantom results of Multitasking and the references. Multitasking produces co-registered T1/T2/T1ρ maps with good image quality. Multitasking T1/T2/T1ρ measurements are in substantial quantitative agreement with reference measurements, as demonstrated by the high R^2 and ICC. The solid line represents identity (y=x) and the dotted line represents linear regression fitting.

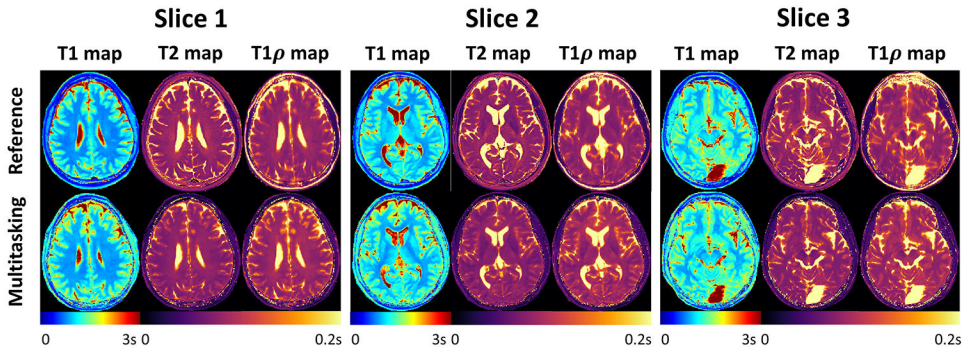

Figure 3.

Example T1/T2/T1ρ maps generated by Multitasking and the reference methods in a healthy control. Multitasking maps show good image quality and are comparable with reference maps.

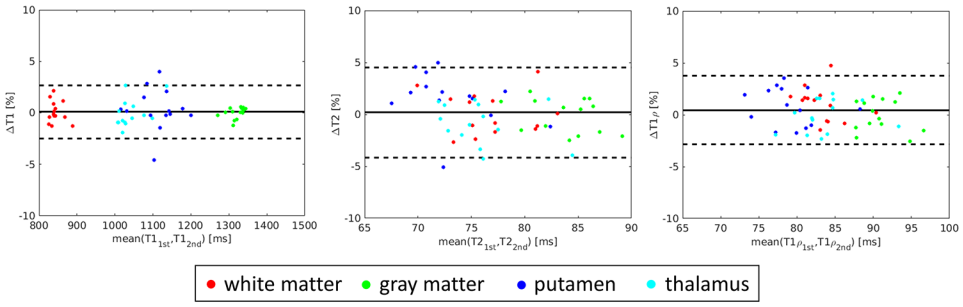

Figure 4.

Bland-Altman analysis for the evaluation of scan-rescan repeatability of the 1st and 2nd Multitasking scans. Left to right: T1, T2, and T1ρ. Each tissue compartment corresponds to a single color. The dotted lines represent 95% confidence level. The solid lines represent mean percentage differences.

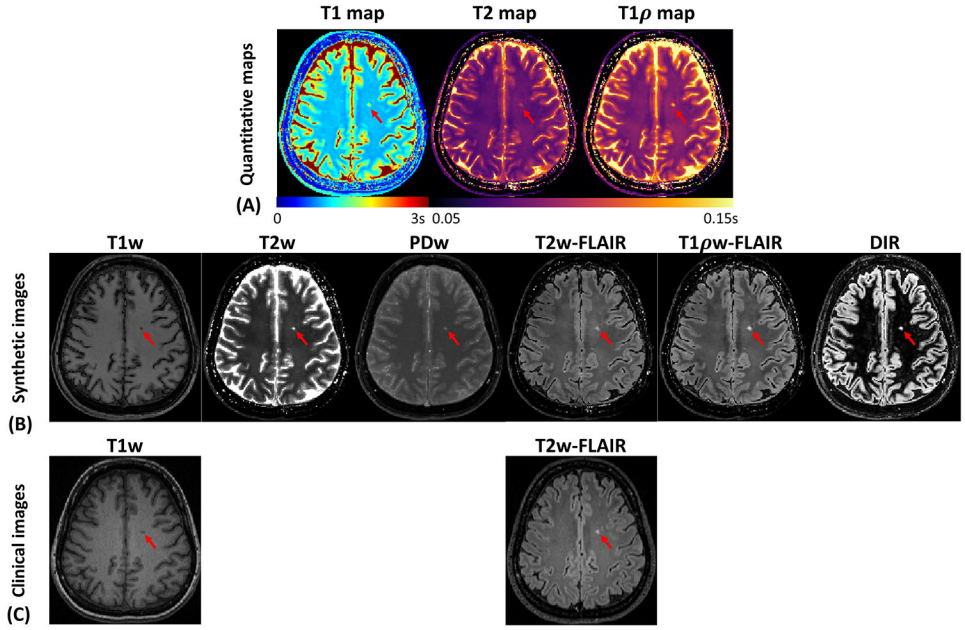

Figure 5.

Clinical demonstration of a 56-year-old female RRMS patient with 20 years disease duration. (A) Multitasking T1/T2/T1ρ maps. (B) Synthetic T1w, T2w, PDw, T2w-FLAIR, T1ρw-FLAIR, and DIR images. (C) Clinical T1w and T2w-FLAIR images (the only clinical images available) which are comparable with the synthetic images. One white matter lesion (red arrow) is clearly delineated on both quantitative maps and synthetic images, among which T1ρ shows better lesion contrast than T2. T2w-FLAIR, T1ρw-FLAIR, and DIR show better lesion contrast with nulled CSF than T1w, T2w, and PDw.

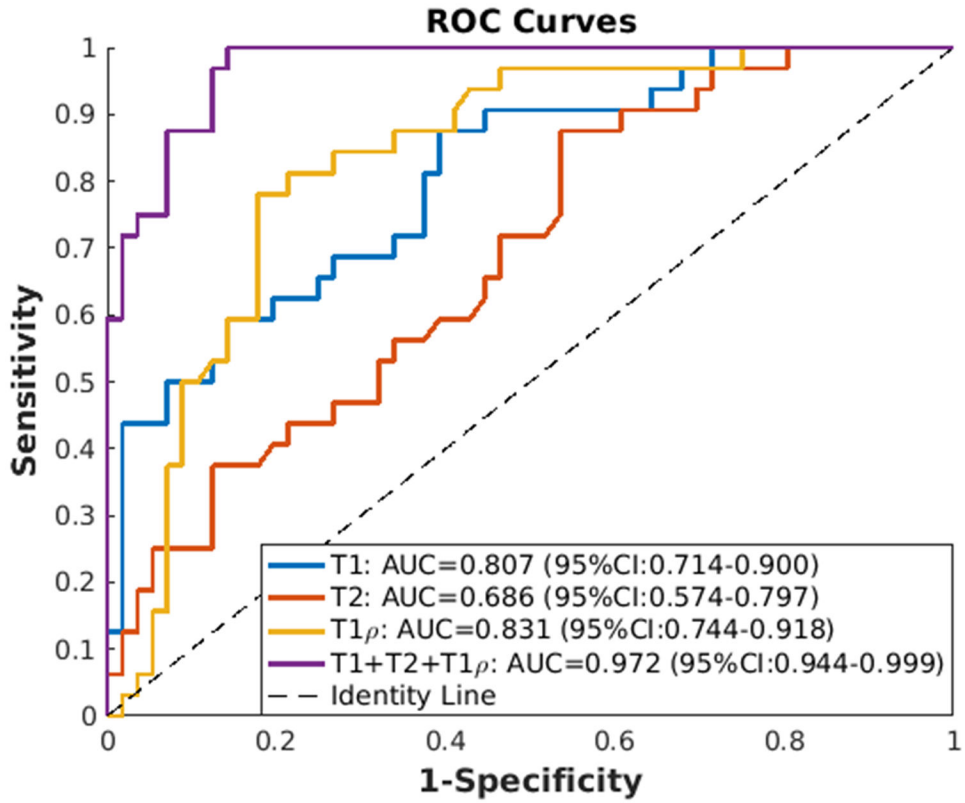

Figure 6.

Receiver operation characteristic (ROC) curves in differentiating RRMS patients with healthy controls, using either single parameter or the combination of three parameters. The area under the curve (AUC) are: T1: AUC=0.807 (95%CI: 0.714-0.900), T2: AUC=0.686 (95%CI: 0.574-0.797), T1ρ: AUC=0.831 (95%CI: 0.744-0.918), T1+T2+T1ρ: AUC=0.972 (95%CI: 0.944-0.999). The dotted line represents identity reference line.

Table 1.

T1/T2/T1ρ measurements of *N*=14 healthy controls using Multitasking and the reference methods.

Healthy Control Measurements (N=14)		White Matter	Cortical Gray Matter	Putamen	Thalamus
Reference Measurements	T1 (ms)	789.6±22.6	1210.8±31.0	1051.8±46.5	987.2±32.7
	T2 (ms)	78.5±3.5	85.3±3.9	74.3±3.8	78.6±3.8
	T1ρ (ms)	80.4±3.3	88.9±3.4	76.1±3.8	81.4±3.6
Multitasking Measurements	T1 (ms)	843.6±18.3	1319.8±28.9	1110.3±43.3	1041.5±34.1
	T2 (ms)	75.9±2.8	83.9±3.6	72.0±3.6	76.0±3.5
	T1ρ (ms)	82.7±3.2	90.9±3.0	77.6±2.7	83.7±3.8

Table 2.

Intraclass correlation coefficients between reference and Multitasking T1/T2/T1ρ measurements in four tissue compartments.

		White Matter	Cortical Gray Matter	Putamen	Thalamus
ICC (Reference vs Multitasking)	T1	0.86	0.90	0.92	0.92
	T2	0.88	0.87	0.85	0.84
	T1ρ	0.87	0.83	0.86	0.81

Table 3.

Intraclass correlation coefficients between the 1st and 2nd Multitasking scans in four tissue compartments.

		White Matter	Cortical Gray Matter	Putamen	Thalamus
ICC (Multitasking 1st vs 2nd)	T1	0.91	0.96	0.93	0.95
	T2	0.94	0.93	0.90	0.92
	T1ρ	0.93	0.94	0.94	0.96

Table 4.

Patient T1/T2/T1ρ measurements in four tissue compartments. Statistical significance against healthy controls (HC) is evaluated. Asterisk (*) indicates significant difference (p<0.05).

RRMS Patients Measurements (N=8)	White Matter	Cortical Gray Matter	Putamen	Thalamus
T1 (ms)	900.1±13.0	1333.9±28.1	1095.7±36.9	1017.3±22.2
P-value vs. HC	$3.9x10^{-7}$*	0.179	0.498	0.102
T2 (ms)	78.7±1.9	86.5±1.3	73.2±1.7	77.8±2.4
P-value vs. HC	0.019*	0.063	0.409	0.850
T1ρ (ms)	86.9±2.5	95.8±3.0	80.5±2.1	86.5±2.5
P-value vs. HC	0.005*	0.001*	0.016*	0.024*